Characterization of the cortical myeloarchitecture with inhomogeneous magnetization transfer imaging (ihMT)

Fanny Munsch, Gopal Varma, Manuel Taso, Olivier M. Girard, Arnaud Guidon, Guillaume Duhamel, David C Alsop

NeuroImage 225 (2021) 117442

Contents lists available at ScienceDirect

NeuroImage

journal homepage: www.elsevier.com/locate/neuroimage

Characterization of the cortical myeloarchitecture with inhomogeneous magnetization transfer imaging (ihMT)

Fanny Munsch[a,*], Gopal Varma[a], Manuel Taso[a], Olivier Girard[b], Arnaud Guidon[c], Guillaume Duhamel[b], David C Alsop[a]

[a] Division of MRI Research, Department of Radiology, Beth Israel Deaconess Medical Center, Harvard Medical School, MA, USA
[b] Aix Marseille Univ, CNRS, CRMBM, Marseille, France
[c] Global MR Applications and Workflow, GE Healthcare, Boston, MA, USA

ARTICLE INFO

Keywords:
MRI
Inhomogeneous magnetization transfer
Magnetization transfer
Cortex
Myelin
Myeloarchitecture

ABSTRACT

Background: Myelin specific imaging techniques to characterize white matter in demyelinating diseases such as multiple sclerosis (MS) have become an area of increasing focus. Gray matter myelination is an important marker of cortical microstructure, and its impairment is relevant in progressive MS. However, its assessment is challenging due to its thin layers. While myelin water imaging and ultra-short TE imaging have not yet been implemented to assess cortical myeloarchitecture, magnetization transfer (MT) shows promise. A recent development of the MT technique, ihMT, has demonstrated greater myelin sensitivity/specificity. Here we implemented a 3D ihMT acquisition and analysis to characterize cortical gray matter myeloarchitecture.

Methods: 20 young healthy volunteers were imaged with a 3D ihMTRAGE sequence and quantitative metrics of ihMT (ihMTsat), and dual frequency-offset MT (dual MTsat) were calculated. Cortical surface-based analysis of ihMTsat and dual MTsat were performed and compared. We also compared the cortical ihMTsat map to a cortical surface-based map of T_1-weighted images (T_1w), defined as a proxy of myelin content.

Results: Cortical ihMTsat and dual MTsat maps were in qualitative agreement with previous work and the cortical T_1w map, showing higher values in primary cortices and lower values in the insula. IhMTsat and dual MTsat were significantly correlated but with important regional differences. The ratio ihMTsat/dual MTsat highlighted higher ihMTsat values in the primary cortices and sulci.

Conclusion: ihMTsat, a quantitative metric of ihMT, can be reliably measured in cortical gray matter and shows unique contrast between cortical regions.

1. Introduction

Differences in cortical microstructure can be reflective of function, neuroanatomy, and pathology. A century of research has emphasized the density and distribution of myelin as a particularly valuable marker. The Vogt school pioneered the field of myeloarchitectonics and showed histologically that myelin content varies from one cortical region to another. They used these regional differences to parcellate the cortex and build the first myeloarchitectonic maps (Braitenberg, 1962; Nieuwenhuys, 2013). The capabilities of noninvasive imaging offer the possibility of in-vivo studies to assess cortical gray matter (GM) myelination for unbiased 3D mapping, characterization of individual variations, and for the study of development, aging, and disease effects.

A variety of Magnetic Resonance Imaging (MRI) modalities have shown sensitivity to cortical myelin. Proposed contrasts have included T_1-weighted (T_1w) images (Rowley et al., 2015) or quantitative T_1 (or R_1) mapping (Sereno et al., 2013; Sprooten et al., 2019), T_2^*-weighted (T2*w) images (Cohen-Adad et al., 2012), quantitative susceptibility mapping (QSM) (Marques et al., 2017) or the T_1w/T_2w ratio (Glasser and Van Essen, 2011; Shafee et al., 2015). These methods have shown a spatial distribution in qualitative agreement with histology; patterns which mostly highlighted primary cortices, known to be heavily myelinated. Nevertheless, these contrasts are not solely sensitive to myelin. Factors such as water density and iron, typically in the form of ferritin, also affect their signal. T_2w, QSM, and T_2^*w images are particularly sensitive to iron, which is often colocalized with myelin (Fukunaga et al., 2010). Using a more specific myelin imaging technique would be of interest. Myelin Water Imaging (MWI) (Alonso-Ortiz et al., 2015), and more specifically Myelin Water Fraction (MWF) MRI, has been mostly used to study myelin in white matter (WM). Only regions of interest analyses have been performed so far in cortical GM (Dvorak et al., n.d.; Prasloski et al., 2012). Indeed, MWI has not yet provided sufficient signal-to-noise ratio (SNR) to assess cortical myelin content (Lee et al., 2020). An inversion recovery ultrashort echo time (IR-UTE) technique has been proposed to directly image myelin in WM

* Corresponding author.
E-mail address: fmunsch@bidmc.harvard.edu (F. Munsch).

https://doi.org/10.1016/j.neuroimage.2020.117442
Received 21 April 2020; Received in revised form 1 October 2020; Accepted 3 October 2020
Available online 9 October 2020

(Du et al., 2014; Jang et al., 2020), but to the best of our knowledge, whole brain GM myelin imaging with UTE has not been reported.

Magnetization Transfer Imaging (MTI) is an alternative myelin sensitive imaging technique that reflects exchange of magnetization between macromolecules, including myelin, and free water. A cortical surface-based study using the magnetization transfer ratio (MTR) has shown promise regarding assessment of cortical myelin content (Mangeat et al., 2015), with results qualitatively in agreement with prior work using other myelin-sensitive contrasts. However, all macromolecules other than those found in myelin contribute to MT contrast, and hence its molecular and diagnostic specificities are reduced, as for example in MS (Moll et al., 2011).

Inhomogeneous magnetization transfer (ihMT) (Varma et al., 2015), a novel variant of MT, can selectively image tissues with long dipolar relaxation time (T_{1D}) components, such as myelin. The ihMT signal is the difference between the MT signal obtained after single off-resonance frequency saturation of the macromolecular pool, and the one obtained after dual symetric off-resonance frequency saturation using the same RF power. The sensitivity of ihMT to local dipolar order and the ordered structure of multiple lipid bilayers underlying myelin (Manning et al., 2017; Swanson et al., 2017; Varma et al., 2015) explains the selective ihMT signal from WM (Girard et al., 2015) and ihMT as a potential biomarker of myelin in WM. This selectivity was further validated by correlation with histological fluorescence microscopy (Duhamel et al., 2019). A strong correlation between ihMT and myelin water imaging measures has also been reported (Ercan et al., 2018; Geeraert et al., 2018). But ihMT has not yet been applied to characterize the cortex and assess its myelin density.

The aim of this work is to assess whether ihMT can be a valuable tool to observe and quantify cortical myelin content. To answer this question, we implemented a 1.6 mm 3D ihMTRAGE sequence, composed of ihMT preparations combined with a rapid gradient echo (RAGE) sequence (Varma et al., 2020). We built cortical surface-based maps of ihMTsat, a quantitative metric of ihMT, and compared them to cortical surface-based maps of T_1w images, previously proposed as a proxy of cortical myelin content. To gain a better understanding of the unique sensitivity of ihMT to cortical myelin, we also compared cortical surface-based maps of ihMTsat to those created using the metric of a more conventional MT technique based on the dual-offset saturation, dual MTsat. Finally, we took a first look at the depth dependence of ihMTsat and dual MTsat.

2. Materials and methods

2.1. MRI acquisition

The study was approved by our institutional review board and informed consent was obtained from each volunteer before enrollment. Twenty young healthy volunteers (range, 20 – 34 years; mean, 27.7 ± 4.7, 12 females) were recruited and scanned on a 3 tesla Discovery MR750 scanner (GE Medical Systems, Milwaukee, WI, USA) with a 32-channel phased-array head coil (Nova Medical, Wilmington MA, USA) for signal reception.

All subjects were scanned with an identical protocol. First, a 3D T_1-weighted inversion prepared gradient echo sequence (GE BRAVO) was acquired for anatomic localization, cortical segmentation using the following parameters: 166 axial slices; 1 mm isotropic resolution; matrix, 256 × 256; TE, 3.2 s; TR, 8.2 s; TI, 450 ms; flip-angle (FA), 12°. Phased array UnifoRmity Enhancement (PURE) was applied to correct for non-uniform receiver coils profile. This 3D $1mm^3$ T_1w BRAVO corrected for B_1 inhomogeneity with PURE was defined as a proxy of myelin content and refers to 'T_1w' in the text. A 3D Fast-Spin-Echo with variable flip-angles (CUBE) T_2-weighted sequence was acquired for robust brain extraction with the following parameters: 196 sagittal slices; resolution, $1mm^3$; matrix, 256 × 256; TE, 120 ms; TR, 4800 ms. Next, a recently described (Varma et al., 2020) 3D ihMTRAGE sequence composed of an ihMT preparation (5 ms off-resonance Tukey-shaped pulses (cosine-modulated for dual-frequency irradiation), Δf=±7 kHz, single-frequency $B_{1,peak}$=14μT, RF pulses every 100 ms for 1 s) combined with an MPRAGE sequence (radial-fan beam view-ordering; 1.6 mm isotropic resolution, matrix, 160 × 160; 90 readouts per $TR_{ihMTRAGE}$; TE, 1.8 ms; TR, 4.6 ms; $TR_{ihMTRAGE}$, 2 s; FA=10°). For enhanced SNR considerations, three repetitions of the single positive (+Δf) and negative (-Δf) frequency-offset images and 6 repetitions of the dual (±Δf) frequency-offset images, all required to compute the ihMT composite image, were acquired. For quantification purpose, two reference images were also acquired at the beginning of the acquisition. The combined MT and reference image acquisition required a total of 20 min. The first reference image was acquired without any off-resonance pulses, and the second one substituted the ihMT preparation with RF spoiled FA=25° pulses applied on-resonance every 25 ms for 1 s. Finally, a quick low resolution (matrix, 64 × 64; slice thickness, 6.4 mm) B_1 map was acquired with a previously described Bloch-Siegert sequence (Sacolick et al., 2010) in 2 min.

2.2. MRI data processing and surface-based analysis

The quantitative analysis procedure involved three steps: preprocessing, derivation of quantitative ihMT and MT metrics, and evaluation of these quantitative metrics across the cortex using cortical surface-based analysis.

2.2.1. Preprocessing of MT and B_1 images

The 3D ihMTRAGE images were preprocessed as follows: (1) realignment of each MT-weighted volume to the reference volume without RF saturation, M_0, using a 6 degree of freedom rigid registration; (2) registration of the reference volume (M_0) to the 3D T_1w volume using rigid registration; (3) application of the saved rigid transformation to the MT-weighted volumes. These preprocessing steps were all performed with FSL (FMBRIB, Oxford, UK).

Using MATLAB (R2017a, MathWorks, Natick, MA, USA) and SPM12 (Statistical Parametric Mapping, Welcome Trust Center for Neuroimaging, London, UK), the Bloch-Siegert B_1 maps were first median filtered with a 21 mm kernel, scaled by a factor of 0.95 to adjust for overestimation of B_1 that occurs when a non-spoiled gradient echo acquisition is used (Corbin et al., 2019) and also registered to the 3D T_1w using the native T_1w gradient echo images of the B_1 sequence to derive the anatomic registration.

The 3 repetitions of single frequency-offset +Δf and -Δf images and the 6 repetitions of the dual frequency-offset images were averaged before quantification of ihMT and MT.

2.2.2. Quantification approach for ihMT and dual MT

We adapted the MT saturation approach from Helms et al. (2008), Helms and Piringer (2005) to derive quantitative ihMT and MT (based on the dual frequency-offset saturation) metrics, unbiased from T_1 and B_1 and independent of sequence timing effects. This approach relies on a model which assumes a short pulse and a relatively long TR such that the effect of each pulse can be considered to be a fractional attenuation of the free pool by the factor (1-δ) (*Eq. (1)*).

$$\begin{aligned} M_{zMT}{}' &= M_{zMT}(1-\delta_{MT}) \\ M_{zref}{}' &= M_{zref}\cos\alpha_{ref} \end{aligned} \quad (1)$$

Based on this MT saturation approach, the quantification of ihMT and MT proceeded in several steps. The measured B_1 maps and the two reference images were first fit to determine T_1 in each voxel. Then, the B_1 and T_1 maps were used to determine the saturation parameter, δ, that

fit the attenuation of each MT prepared image relative to the unsaturated image. Finally, the δ values for different experiments were used to calculate the ihMT and MT metrics. For both fits, we constructed a simple forward model for the spoiled gradient echo excitations and the MT preparation RF pulses (or the reference pulses), as a function of T_1 and B_1 and inverted them using a bisection fitting algorithm with guaranteed convergence to determine first T_1 from the reference images, and then δ for each MT preparation. Finally, the MT metrics dual MTsat and ihMTsat were calculated from the δ_{MT} as defined in *Eq. (2)*. Since the MT and ihMT saturation effects scale approximately respectively polynomially and quadratically with RF amplitude for our parameters (Varma et al., 2018), they were scaled to correct for B_1 variations.

$$\begin{aligned} MTsat &= \delta_{MT\pm} / \left(-0.3395 \left(\frac{B_{1act}}{B_{1nom}} \right)^4 + 1.2754 \left(\frac{B_{1act}}{B_{1nom}} \right)^2 + 0.0641 \right) \\ ihMTsat &= \left(\frac{B_{1nom}}{B_{1act}} \right)^2 \left(2\delta_{MT\pm} - \delta_{MT+} - \delta_{MT-} \right) \end{aligned} \quad (2)$$

A more detailed description of this quantification is given in the Appendix.

2.2.3. Surface-based analysis

Each subject's 3D T_1w image was processed using FreeSurfer version 6.0 (http:// surfer.nmr.mgh.harvard.edu) in order to reconstruct the white and pial surfaces and parcellate the cortex. The pipeline did not include skull-stripping which was performed with SPM12, to restrict pial surface manual corrections. Briefly, segmentation of GM, WM and cerebrospinal fluid (CSF) was performed on T_2w images due to its high contrast between the dura mater and GM. The three classes were added to create a skull-stripped T_2w image, which was used afterwards to mask the 3D T_1w image, ihMTsat, dual MTsat and the ratio ihMTsat/dual MTsat. The white surface was also manually corrected for all subjects.

Though all images were already spatially registered, an additional registration of each of the ihMTsat, dual MTsat, ihMTsat/dual MTsat ratio, and T_1w images to the cortical surfaces was performed using boundary-based registration method. Next, image intensities at several cortical depths (from 10% to 90%, every 10%) between white and pial surfaces were measured. In order to correct for receiver gain differences between subjects, we scaled the individual T_1w maps by the corresponding cortical mean value. Then, projection of the maps to an across subject average surface (*fsaverage*), averaging across subjects and smoothing along the surface with a 5 mm FWHM Gaussian kernel were performed.

We also used the quantitative T_1 map (from the B_1 and the two reference images) to generate a R_1 ($1/T_1$) map. We generated cortical surface-based maps of R_1 applying the identical surface-based analysis pipeline described at the start of this subsection.

2.3. Regional analyses

Quantitative comparisons were performed using average values within previously defined cortical regions. We projected the Destrieux cortical atlas from FreeSurfer (Destrieux et al., 2010), composed of 148 Regions of Interest (ROIs, 74 per hemisphere), onto the following cortical surface-based maps previously created: ihMTsat, dual MTsat, ihMTsat/dual MTsat ratio, and T_1w, from which mean values at 50% depth were extracted. To assess the relationships between ihMTsat and T_1w or dual MTsat across the brain, we regressed their 148 mean values and performed Spearman's rank correlations. Moreover, to assess the level of myelination across regions, we performed paired Student t-tests across subjects comparing the ihMTsat value in each region to the median ihMTsat value across the regions. The statistical analyses were performed using R (version 3.5).

Furthermore, we took a first look at the depth dependence behavior of ihMTsat, dual MTsat and ihMTsat/dual MTsat for 7 ROIs from the Destrieux atlas (primary cortices, posterior cingulate), believed to be heavily myelinated, though the nominal resolution is not high enough for a precise analysis. To do so, we extracted the mean values for each metric at every 10% depth level starting from 10% and ending at 90%.

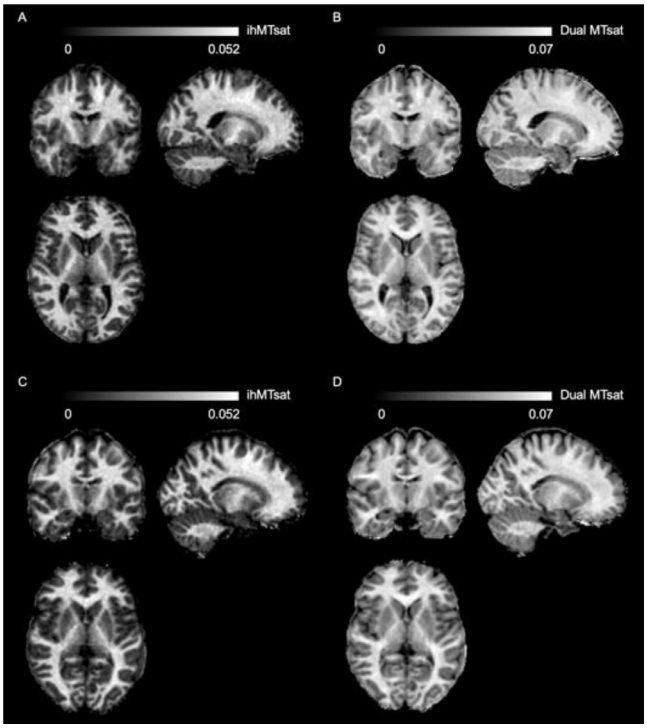

Fig. 1. Examples of quantitative images from a 32-year-old male healthy volunteer – A) ihMTsat and B) Dual MTsat maps and a 23-year-old male healthy volunteer – C) ihMTsat and D) Dual MTsat maps.

This range was chosen to consider the potential contamination of WM and CSF due to partial volume effects. We averaged the values from the left and right hemispheres assuming that the depth dependence behavior is not hemispheric-dependent.

2.4. Data and code availability statement

Anonymized imaging data will be shared upon request from any interested and qualified investigator after completing a Data Sharing Agreement with Beth Israel Deaconess Medical Center.

The quantitative MTsat / ihMTsat code will be shared upon request from any interested and qualified investigator.

3. Results

All ihMTsat and dual MTsat maps were of good quality and free of obvious visually apparent artifacts (*Fig. 1*). A good WM/GM contrast for both maps, albeit more pronounced for ihMTsat, was observed. The corticospinal tract, a heavily myelinated white matter tract, is very bright and highly recognizable on the ihMTsat map.

3.1. Assessment of cortical myelin density distribution with ihMTsat

Cortical ihMTsat, sampled at mid-distance between white and pial surfaces, was higher in the primary motor cortices (central sulcus (*S_sulcus*), pre- and postcentral gyri (*G_precentral* and *G_postcentral*)), the primary visual areas such as MT (also called V5) (*S_occipital_ant*), V1 and V2 (*S_calcarine, G_cuneus*), and the primary auditory cortex (*G_temp_sup-G_T_transv*). These elevations relative to the median were respectively significant at p <0.0001 for *S_sulcus, G_precentral, S_occipital_ant* and *G_temp_sup-G_T_transv*, p <0.002 for *G_postcentral* and $p = 0.04$ for the left *G_cuneus*. Conversely, the insula (*G_insular_short*), known to be lightly myelinated (Glasser and Van Essen, 2011), had low ihMTsat, with a significant reduction relative to the median for *G_insular_short* (p <0.0001).

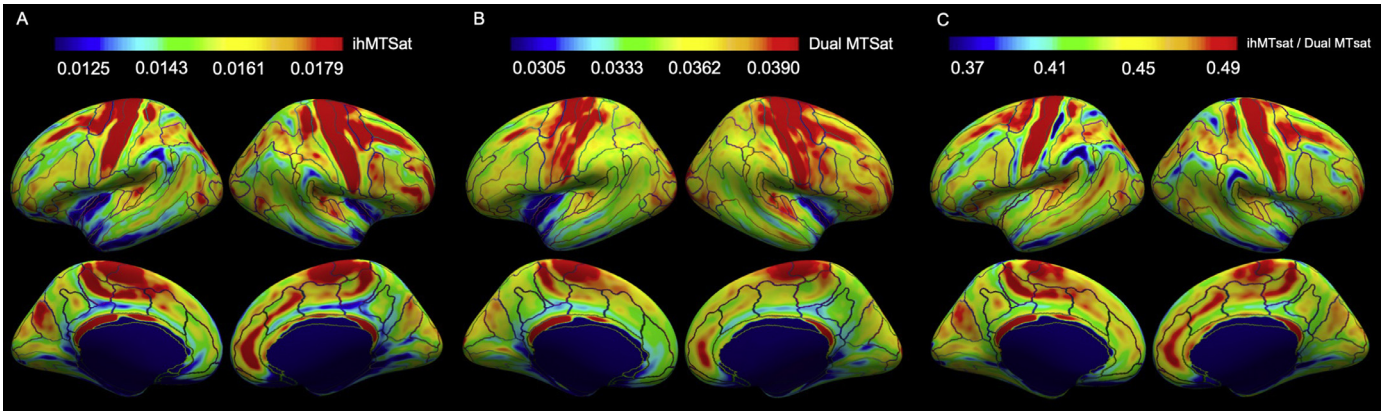

Fig. 2. Cortical surface-based maps of quantitative MT based measures sampled at mid-distance between the white and pial surfaces and averaged across 20 healthy volunteers A) Cortical ihMTsat, B) Cortical dual MTsat and C) Cortical ratio of ihMTsat/dual MTsat.

The signal intensities are more variable for association areas. (*Fig. 2-A, Supplementary Tables 1&2*).

3.2. Relationship between ihMTsat and dual MTsat

Cortical surface-based ihMTsat and dual MTsat maps show a close spatial distribution (*Fig. 2-A, Fig. 2-B, Supplementary Table 1*), which is further supported by the strong spatial correlation between ihMTsat and dual MTsat values measured in the 74 ROIs of the Destrieux cortical atlas (ρ=0.86, p <0.0001 and ρ=0.85, p <0.0001, respectively for the left and right hemispheres) (*Fig. 3-A*, *Fig. 3-B*). However, some regional differences exist. For example, ihMTsat values are relatively higher in the primary auditory cortex, primary visual areas such as V1 and in the central sulcus than dual MTsat values. Those regional differences are emphasized by the cortical surface-based map of the ratio ihMTsat/dual MTsat (*Fig. 2-C, Supplementary Table 1*). This ratio brings out the unique information carried by ihMT relative to MT and shows interesting features whose boundaries overlap with regional boundaries from the Destrieux atlas. Relative to dual MTsat, ihMTsat generally has higher values in sulci than gyri.

Some significant hemispheric differences are visible in both ihMTsat and dual MTsat. Performing paired *t*-test across subjects adjusted for multiple comparisons across regions, we found significantly higher ihMTsat and MTsat values on the right hemisphere in the anterior cingulate and inferior frontal regions and significantly higher values on the left hemisphere in a few occipital regions (*Supplementary Table 3*).

3.3. A preliminary evaluation of the depth dependence of ihMTsat and dual MTsat

Though our resolution was insufficient to precisely evaluate the laminar depth dependence of ihMT, a preliminary evaluation showed promising differences between ihMT and MT. The decrease of ihMTsat with depth into the cortex follows a two-slope pattern with a rapid decrease from the white surface to 50% depth followed by a slower decrease from the mid-distance to the pial surface in almost every chosen ROI (*Fig. 4-A, Supplementary Table 4*). Conversely, the dual MTsat decrease does not follow a specific pattern (*Fig. 4-B, Supplementary Table 5*). Especially dual MTsat values in both precentral and postcentral gyri seem to decrease faster closer to the GM. The ratio ihMTsat/dual MTsat follows a similar, but more prominent, two-slope pattern as ihMTsat (*Fig. 4-C, Supplementary Table 6*).

3.4. Relationship of ihMT to cortical variation of T_1-weighted signal

T_1-weighted signal intensity also varied considerably across cortical regions. Primary cortices (primary motor cortex, primary visual areas, primary auditory cortex) have higher T_1w intensities than the rest of the brain (*Fig. 5-B, Supplementary Table 1*), a feature also visible on ihMTsat map (*Fig. 5-A, Supplementary Table 1*). However, T_1w and ihMTsat differed considerably in spatial distribution in other regions, as supported by the absence of spatial correlations between ihMTsat and T_1w values measured in the 74 ROIs of the Destrieux cortical atlas (ρ=0.05, p = 0.7and ρ=−0.06, p = 0.6, respectively for the left and right hemispheres) (*Fig. 3-C*, *Fig. 3-D*).

In addition to the T_1w signal, we also obtained T_1 information from the T_1 maps that were part of our ihMTsat quantification approach. These can also be compared to ihMTsat. As described in the Appendix, these T_1 maps are very sensitive to errors in the measured B_1. Our B_1 mapping procedure, using an unspoiled Bloch-Siegert method, has been shown to overestimate B_1, especially in CSF (Corbin et al., 2019), raising questions about the T_1 map reliability. Fortunately, the ihMTsat and MTsat measures are much less vulnerable to this error (see Appendix). For completeness, we have included correlations between R_1 measured from the T_1 maps and our other measures (*Supplementary Fig. 1*) and the cortical surface-based map of R_1 (*Supplementary Fig. 2*) in supplementary data.

4. Discussion

These results highlight both the sensitivity of ihMT, enabling robust imaging at spatial resolution sufficient to resolve the cortex, and its specificity to cortical myeloarchitecture. The ihMT signal is believed to mainly reflect lipid membrane density (Duhamel et al., 2019), which is very high in myelinated tissue. Myelin density is also known to be an important indicator of cortical architecture (Nieuwenhuys, 2013) with higher myelination in primary cortices. Hence, our finding of higher ihMTsat in primary motor, auditory, and visual cortices is consistent with the myeloarchitecture of the cerebral cortex.

Though ihMT shared strong similarities to a more conventional MT measure, as supported by the strong correlations between ihMTsat and dual MTsat across regions, clear regional differences exist and are highlighted by the cortical surface-based map of the ratio ihMTsat/dual MTsat. Both contrasts are sensitive to myelin but since MT is also equally sensitive to other tissue macromolecules, (Duhamel et al., 2019), this ratio likely provides an indication of the fractional myelin content. IhMTsat shows higher relative values compared to dual MTsat in primary cortices (primary motor cortex, primary visual areas and primary auditory cortex). Even outside the primary cortices, the ratio ihMTsat/dual MTsat shows an interesting pattern, which follows the boundaries of the Destrieux atlas (based on separation of gyral and sulcal regions) from FreeSurfer (Destrieux et al., 2010). Higher ihMTsat/dual MTsat is mainly located in sulci. Neuroanatomical studies have generally shown a thicker but less densely myelinated layer of the cortex in

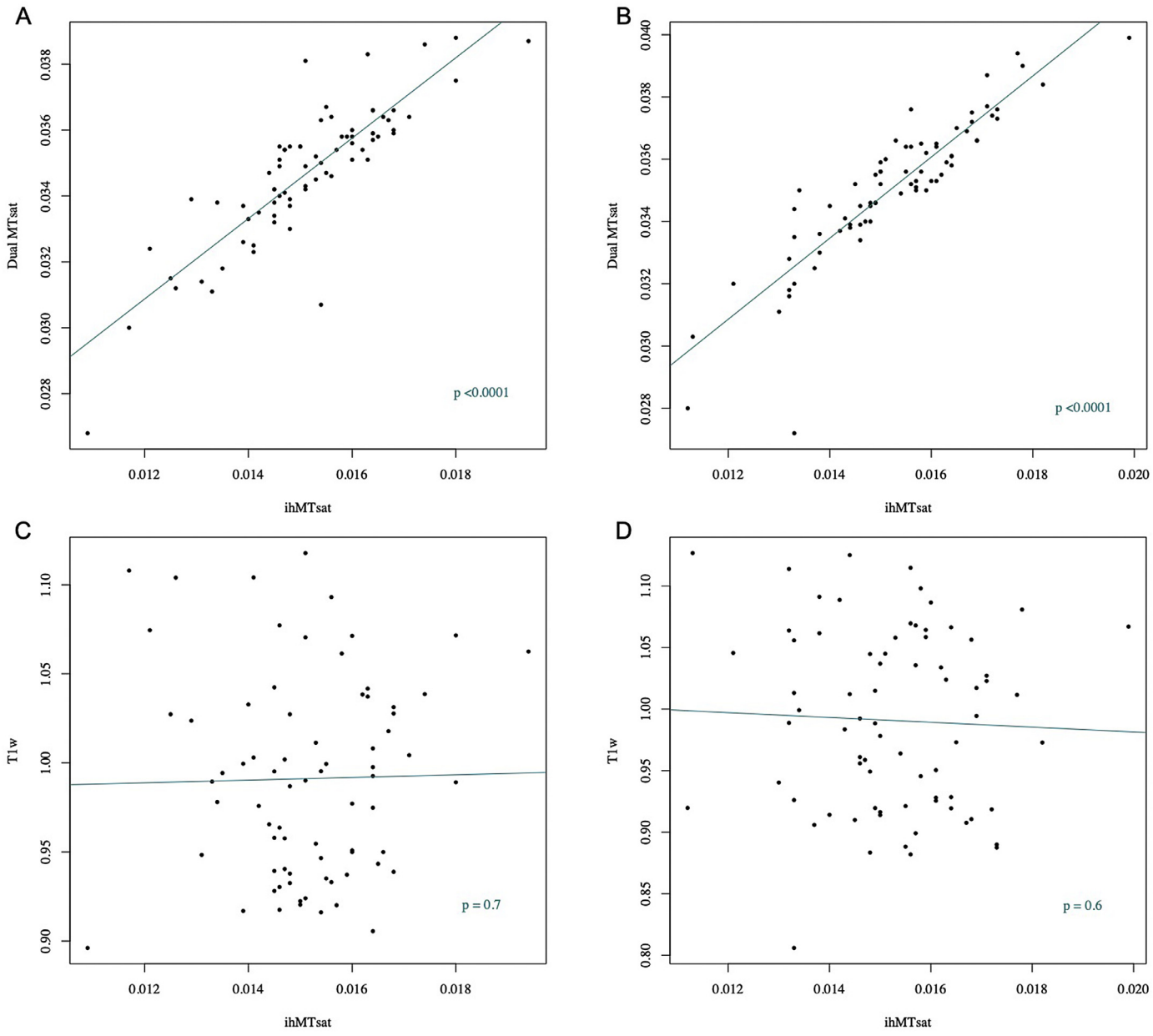

Fig. 3. Regression between ihMTsat and dual MTsat at 50% depth in the left (A) and right (B) hemispheres, and between ihMTsat and T_1w at 50% depth in the left (C) and right (D) hemispheres.

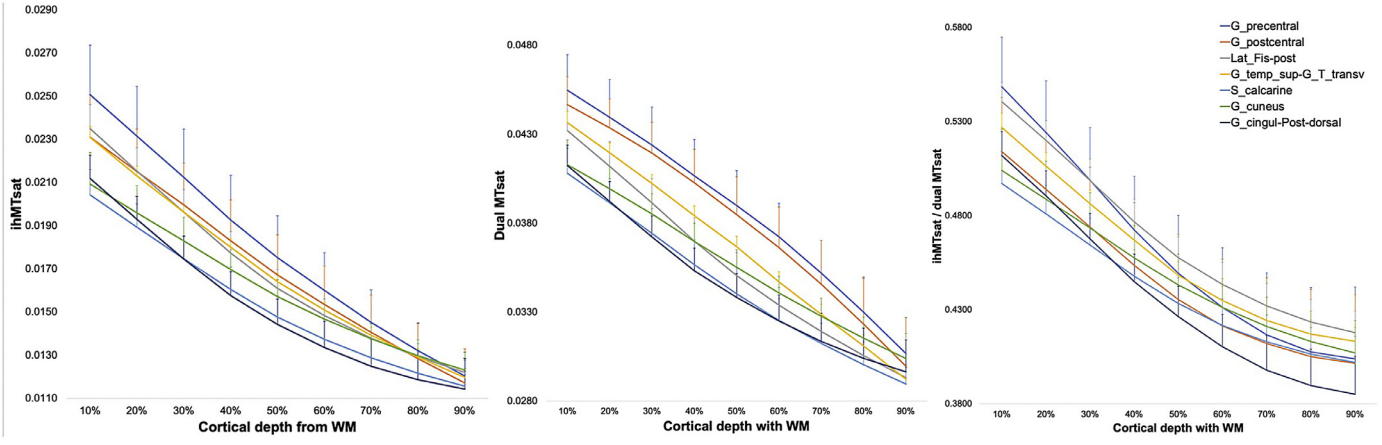

Fig. 4. Preliminary evaluation of cortical depth dependence of MT related measures: ihMTsat (A), dual MTsat (B) and ihMTsat/dual MTsat (C).

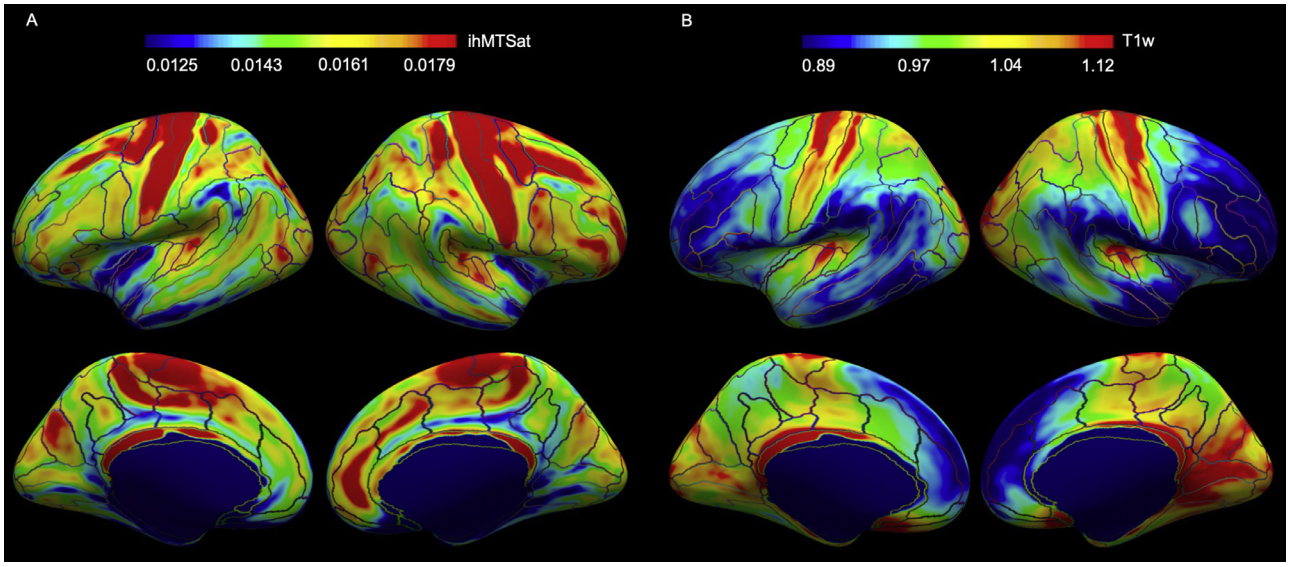

Fig. 5. A) Cortical ihMTsat and B) T_1w maps sampled at mid-distance between the white and pial surfaces and averaged across 20 healthy volunteers

sulci (Hilgetag and Barbas, 2006; Horiuchi-Hirose and Sawada, 2016). Spatial differences are also observed in cortical depth dependence, with ihMTsat decreasing more rapidly than dual MTsat with distance from the white matter surface. Further study of the depth dependence at higher spatial resolution is nevertheless needed to better probe the depth dependence of these measures and to clarify this relationship. Though the physical and anatomical basis of gyral-sulcal and depth dependent contrast will require further study, it does highlight the unique information available from ihMT for microstructural analysis and differentiation of cortical regions.

This work adds to a growing literature on MRI characterization of gray matter microstructural heterogeneity. Previous work with T_1w/T_2w and T_1w contrasts (Glasser and Van Essen, 2011; Rowley et al., 2015; Sereno et al., 2013; Sprooten et al., 2019) has emphasized the prominence of primary cortices, and these findings are reproduced with our T_1w analysis here. Though primary cortices are also prominent in the ihMTsat measure, the intensity of the contrast and the distribution of the signal across the entire cortex is quite different, resulting in a poor correlation across the regions of the Destrieux atlas. This lack of correlation has previously been reported in WM between T_1w/T_2w and another myelin-sensitive MRI technique, myelin water imaging (Arshad et al., 2017; Uddin et al., 2018). Both teams suggested that compared to myelin water fraction, T_1w/T_2w would represent a more general measure of tissue microstructure, such as variation in caliber and packing density of the axons. This difference could also be partly explained by the sensitivity of T_1w/T_2w to iron. Indeed, iron and myelin are colocalized in the cortex, especially in primary cortices (Edwards et al., 2018; Fukunaga et al., 2010) but this colocalization is imperfect (Fukunaga et al., 2010). Using quantitative magnetic susceptibility (QSM) and conventional MT, Marques et al. created a model to separate signals from myelin and iron and reconstructed a myelin map and an iron map (Marques et al., 2017). The iron map shows higher iron content mostly in primary cortices, similar to a T_1w/T_2w map, while the patterns of the myelin map and our ihMTsat map are more similar.

This initial study of cortical ihMT is not without limitations. Importantly, the spatial resolution of 1.6 mm is higher than the average cortical thickness but low enough that partial volume effects may contribute to the analysis. This is especially true in the thinner cortex of the primary visual cortex. However, comparison of the regional distribution of cortical thickness and our MT measures yielded low correlation (R^2 <0.3) (Supplementary Fig. 3), suggesting this is not a major problem for our mid-thickness analysis. The analysis of cortical thickness dependence of the MT and ihMT measures is almost certainly affected at some level by partial volume effects. Such effects could blur higher resolution structure and also include some signal from nearby white matter, which has previously been shown to vary with cortical region and age (Salat et al., 2009). Still the differences between MT and ihMT depth profiles observed in this preliminary analysis, that should be equally affected by partial volume, suggest unique sensitivity of ihMT to cortical microstructure.

Though a vendor correction for surface coil nonuniformity was applied to our T_1w image, it was still imperfectly corrected for biases related to transmit field inhomogeneity. Our primary focus was to characterize ihMT and MT distribution and the T_1w image was acquired primarily for tissue segmentation. Improved methods for bias correction and especially quantification of T_1 are recommended for studies of cortical contrast. However, we included results from our T_1w images knowing this drawback and the resolution effect ($1mm^3$ versus 1.6 mm isotropic) because they showed similar contrast to earlier work using T_1 contrast in the cortex and could readily be displayed on the same subject atlas.

Our MTsat measure differs significantly from measures in other MT studies and care should be taken in direct comparison. We used a high frequency offset for the MT saturation, 7 kHz, compared to most MT studies that use 2 kHz or lower. More recently, however, higher offset frequencies have been advocated to remove bound pool T_2 effects in quantitative MT studies (Yarnykh et al., 2014). Additionally, we used brief pulses with longer repetition times to increase the ihMT signal (Varma et al., 2018). Indeed, with these high-power pulses, the MTsat is no longer linear in applied power. Finally, we used a quantitative MTsat measure that differs substantially from the more conventional MT ratio. For all these reasons, our findings may differ from those obtained with other methods.

Another challenge is that understanding of and quantification methods for ihMT are rapidly evolving, making comparison across studies difficult. Recent work has emphasized the presence of a distribution of dipolar relaxation times in tissue (Carvalho et al., 2020) which can be differentially emphasized by the sparseness and intensity of the applied power (Mchinda et al., 2018; Varma et al., 2018) and by the choice of dipolar relaxation time weighting in the dual frequency saturation (Carvalho et al., 2020; Duhamel et al., 2019; Prevost et al., 2017; Varma et al., 2018). While standardization of methods is clearly important, the ability to characterize different tissue components by vary-

ing the saturation opens up new possibilities for the study of tissue microstructure.

5. Conclusion

This work has demonstrated that ihMT, previously emphasized in studies of white matter, can provide unique and potentially important quantification of cortical gray matter. The results can complement the findings of other approaches in studies of normal myeloarchitecture and provide a new quantitative measure for pathology in diseases that affect gray matter, including progressive multiple sclerosis and Alzheimer's disease.

Declaration of Competing Interest

D.C.A. receives research support from GE Healthcare. Additionally, he receives postmarket royalties through his institution from GE Healthcare, Siemens Healthineers, Philips Medical, Hitachi, and Animage LLC for patents related to the PCASL technique.

Supplementary materials

Supplementary material associated with this article can be found, in the online version, at doi:10.1016/j.neuroimage.2020.117442.

Appendix

MTsat and T_1 were quantified using the following model (Fig. A1).

The effect of a RF pulse applied on-resonance at time 0 followed by a wait, T_{rp}, on the equilibrium longitudinal magnetization, is given by:

$$M_z(T_{rp}) = M_z(0)\cos\alpha e^{-\frac{T_{rp}}{T_1}} + M_0\left(1 - e^{-\frac{T_{rp}}{T_1}}\right) \quad \text{(A1)}$$

After n pulses, the magnetization is given by

$$M_z(nT_{rp}) = M_z(0)\cos^n(\alpha)e^{-\frac{nT_{rp}}{T_1}} + M_0\left(1 - e^{-\frac{T_{rp}}{T_1}}\right)\sum_{k=0}^{n-1}\cos^k(\alpha)e^{-\frac{kT_{rp}}{T_1}} \quad \text{(A2)}$$

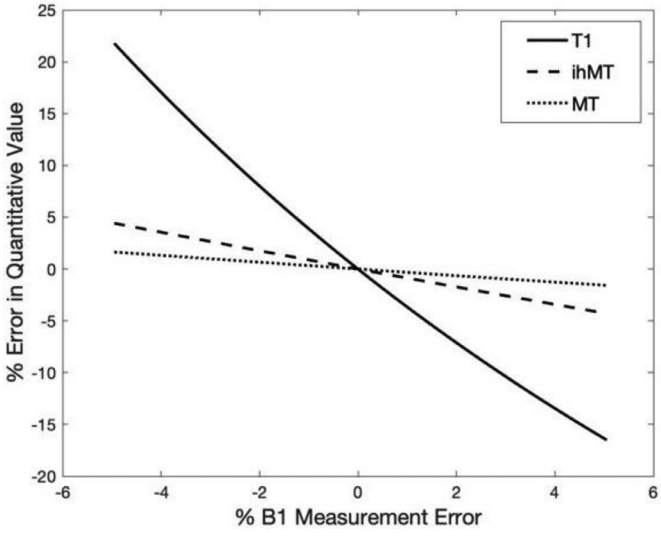

Fig. A1. Simulation of the quantification error for T_1, δ_{ihMT}, δ_{MT} as a function of the error in measurement of B_1. T_1 of 1.4 s and true B_1 of 2.4μT was assumed. T_1 is much more affected by errors in the B_1 measurement than the MT measures.

Or

$$M_z(nT_{rp}) = M_z(0)\cos^n(\alpha)e^{-\frac{nT_{rp}}{T_1}} + M_0\left(1 - e^{-\frac{T_{rp}}{T_1}}\right)\frac{\left(1 - \cos^n(\alpha)e^{-\frac{nT_{rp}}{T_1}}\right)}{\left(1 - \cos(\alpha)e^{-\frac{T_{rp}}{T_1}}\right)}$$

In the limit of large n, small flip angle α and short T_{rp}, this becomes

$$M_z(nT_{rp}) \approx M_0\frac{\left(1 - e^{-\frac{T_{rp}}{T_1}}\right)}{\left(1 - \cos(\alpha)e^{-\frac{T_{rp}}{T_1}}\right)} \approx M_0\frac{1}{\left(1 + \frac{\alpha^2 T_1}{2T_{rp}}\right)} \quad \text{(A3)}$$

In the MTsat model, the effect of an off-resonance MT pulse repeated every T_{rs} is modeled as a saturation factor, δ.

$$M_z(T_{rs}) = M_z(0)(1-\delta)e^{-\frac{T_{rs}}{T_1}} + M_0\left(1 - e^{-\frac{T_{rs}}{T_1}}\right) \quad \text{(A4)}$$

Similarly,

$$M_z(nT_{rs}) = M_z(0)(1-\delta)^n e^{-\frac{nT_{rs}}{T_1}} + M_0\left(1 - e^{-\frac{T_{rs}}{T_1}}\right)\frac{\left(1 - (1-\delta)^n e^{-\frac{nT_{rs}}{T_1}}\right)}{\left(1 - (1-\delta)e^{-\frac{T_{rs}}{T_1}}\right)}$$

And for n large, δ small, and T_{rs} short,

$$M_z(nT_{rs}) \approx M_0\frac{\left(1 - e^{-\frac{T_{rs}}{T_1}}\right)}{\left(1 - (1-\delta)e^{-\frac{T_{rs}}{T_1}}\right)} \approx M_0\frac{1}{\left(1 + \frac{\delta T_1}{T_{rs}}\right)} \quad \text{(A5)}$$

These are identical to the equations for an on-resonance pulse with the substitution

$$\delta = 1 - \cos\alpha = 2\sin^2\left(\frac{\alpha}{2}\right) \approx \frac{\alpha^2}{2} \quad \text{(A6)}$$

In the limit of n large, α and δ small, and T_{rs} short compared to T_1, we can quantify δ from an MT-weighted image using one reference image with zero flip angle (S_0) and one with flip angle α (S_α).

$$\delta = \frac{\alpha^2 T_{rs}}{2T_{rp}}\frac{\left(\frac{1}{S_{mt}} - \frac{1}{S_0}\right)}{\left(\frac{1}{S_\alpha} - \frac{1}{S_0}\right)} \quad \text{(A7)}$$

And if we want to correct δ for B_1 variations proportional to the squared of B_1

$$\delta_{corr} = \delta\left(\frac{\alpha_{\text{nominal}}}{\alpha}\right)^2 = \frac{\left(\alpha_{\text{nominal}}\right)^2 T_{rs}}{2T_{rp}}\frac{\left(\frac{1}{S_{mt}} - \frac{1}{S_0}\right)}{\left(\frac{1}{S_\alpha} - \frac{1}{S_0}\right)} \quad \text{(A8)}$$

We see that using the nominal flip angle already corrects for B_1. This approach removes T_1 and B_1 effects simultaneously and a B_1 map is not needed for quantification of MTsat.

If you have a B_1 map, you can calculate the T_1 from the two reference images.

$$T_1 = \frac{2T_{rp}}{\alpha^2}\left(\frac{S_0}{S_\alpha} - 1\right) \quad \text{(A9)}$$

But this T_1 measurement will be majorly affected by an imperfect B_1 map.

In the case of a shorter preparation such that steady state is not reached, the qualitative behavior is similar but the solution must be calculated numerically by inverting a physical model for the magnetization as a function of T_1 and α or δ. The calculation was performed by stepping across 4 time periods: the wait before the RF preparation, w_p, the preparation time, nT_{rp}, the delay before acquisition, w_d, and the acquisition time, mT_r.

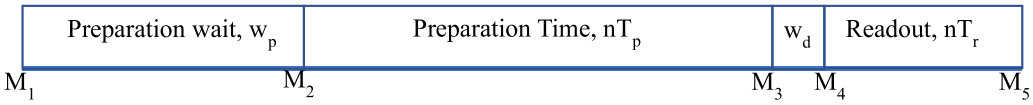

$$
\begin{aligned}
M_2 &= M_1 e^{-\frac{w_p}{T_1}} + M_0\left(1 - e^{-\frac{w_p}{T_1}}\right)\\
M_3 &= M_2\cos^n(\alpha)e^{-\frac{nT_{rp}}{T_1}} + M_0\left(1 - e^{-\frac{T_{rp}}{T_1}}\right)\frac{\left(1-\cos^n(\alpha)e^{-\frac{nT_{rp}}{T_1}}\right)}{\left(1-\cos(\alpha)e^{-\frac{T_{rp}}{T_1}}\right)}\\
M_4 &= M_3 e^{-\frac{w_d}{T_1}} + M_0\left(1 - e^{-\frac{w_d}{T_1}}\right)\\
M_5 &= M_1\cos^m(\beta)e^{-\frac{mT_r}{T_1}} + M_0\left(1 - e^{-\frac{T_r}{T_1}}\right)\frac{\left(1-\cos^m(\beta)e^{-\frac{mT_r}{T_1}}\right)}{\left(1-\cos(\beta)e^{-\frac{T_r}{T_1}}\right)}\\
M_1' &= M_5
\end{aligned}
\tag{A10}
$$

Where β is the readout flip angle, T_r is the readout repetition time and m is the number of readout pulses per segment. For δ, replace $\cos(\alpha)$ with 1-δ and T_{rp} with T_{rs}. For reasonable parameters, the ratio of the reference images is a monotonic function of T_1 and the ratio of the MT image to the 0° reference image is a monotonic function of δ. These can readily be solved at each point of the image by a robust bisection method.

We can simulate the effect of an error in measured B_1 on the measured T_1 and δ. T_1 is strongly affected but δ is much more mildly affected by the error.

References

Alonso-Ortiz, E., Levesque, I.R., Pike, G.B., 2015. MRI-based myelin water imaging: a technical review. Magn. Reson. Med. 73, 70–81. doi:10.1002/mrm.25198.

Arshad, M., Stanley, J.A., Raz, N., 2017. Test–retest reliability and concurrent validity of in vivo myelin content indices: myelin water fraction and calibrated T1w/T2w image ratio. Hum. Brain Mapp. 38, 1780–1790. doi:10.1002/hbm.23481.

Braitenberg, V., 1962. A note on myeloarchitectonics. J. Comp. Neurol. 118, 141–156. doi:10.1002/cne.901180202.

Carvalho, V.N.D., Hertanu, A., Grélard, A., Mchinda, S., Soustelle, L., Loquet, A., Dufourc, E.J., Varma, G., Alsop, D.C., Thureau, P., Girard, O.M., Duhamel, G., 2020. MRI assessment of multiple dipolar relaxation time (T1D) components in biological tissues interpreted with a generalized inhomogeneous magnetization transfer (ihMT) model. J. Magn. Reson. 311, 106668. doi:10.1016/j.jmr.2019.106668.

Cohen-Adad, J., Polimeni, J.R., Helmer, K.G., Benner, T., McNab, J.A., Wald, L.L., Rosen, B.R., Mainero, C., 2012. T2* mapping and B0 orientation-dependence at 7T reveal cyto- and myeloarchitecture organization of the human cortex. Neuroimage 60, 1006–1014. doi:10.1016/j.neuroimage.2012.01.053.

Corbin, N., Acosta-Cabronero, J., Malik, S.J., Callaghan, M.F., 2019. Robust 3D Bloch-Siegert based mapping using multi-echo general linear modeling. Magn. Reson. Med. 82, 2003–2015. doi:10.1002/mrm.27851.

Destrieux, C., Fischl, B., Dale, A., Halgren, E., 2010. Automatic parcellation of human cortical gyri and sulci using standard anatomical nomenclature. Neuroimage 53, 1–15. doi:10.1016/j.neuroimage.2010.06.010.

Du, J., Ma, G., Li, S., Carl, M., Szeverenyi, N.M., VandenBerg, S., Corey-Bloom, J., Bydder, G.M., 2014. Ultrashort echo time (UTE) magnetic resonance imaging of the short T2 components in white matter of the brain using a clinical 3T scanner. Neuroimage 87, 32–41. doi:10.1016/j.neuroimage.2013.10.053.

Duhamel, G., Prevost, V.H., Cayre, M., Hertanu, A., Mchinda, S., Carvalho, V.N., Varma, G., Durbec, P., Alsop, D.C., Girard, O.M., 2019. Validating the sensitivity of inhomogeneous magnetization transfer (ihMT) MRI to myelin with fluorescence microscopy. Neuroimage 199, 289–303. doi:10.1016/j.neuroimage.2019.05.061.

Dvorak, A.V., Wiggermann, V., Gilbert, G., Vavasour, I.M., MacMillan, E.L., Barlow, L., Wiley, N., Kozlowski, P., MacKay, A.L., Rauscher, A., Kolind, S.H., 2020. n.d. Multi-spin echo T2 relaxation imaging with compressed sensing (METRICS) for rapid myelin water imaging. Magn. Reson. Med. doi:10.1002/mrm.28199.

Edwards, L.J., Kirilina, E., Mohammadi, S., Weiskopf, N., 2018. Microstructural imaging of human neocortex in vivo. NeuroImage Microstruct. Imaging 182, 184–206. doi:10.1016/j.neuroimage.2018.02.055.

Ercan, E., Varma, G., Mädler, B., Dimitrov, I.E., Pinho, M.C., Xi, Y., Wagner, B.C., Davenport, E.M., Maldjian, J.A., Alsop, D.C., Lenkinski, R.E., Vinogradov, E., 2018. Microstructural correlates of 3D steady-state inhomogeneous magnetization transfer (ihMT) in the human brain white matter assessed by myelin water imaging and diffusion tensor imaging. Magn. Reson. Med. 80, 2402–2414. doi:10.1002/mrm.27211.

Fukunaga, M., Li, T.-.Q., Gelderen, P.van, Zwart, J.A.de, Shmueli, K., Yao, B., Lee, J., Maric, D., Aronova, M.A., Zhang, G., Leapman, R.D., Schenck, J.F., Merkle, H., Duyn, J.H., 2010. Layer-specific variation of iron content in cerebral cortex as a source of MRI contrast. Proc. Natl. Acad. Sci. 107, 3834–3839. doi:10.1073/pnas.0911177107.

Geeraert, B.L., Lebel, R.M., Mah, A.C., Deoni, S.C., Alsop, D.C., Varma, G., Lebel, C., 2018. A comparison of inhomogeneous magnetization transfer, myelin volume fraction, and diffusion tensor imaging measures in healthy children. NeuroImage Microstruct. Imaging 182, 343–350. doi:10.1016/j.neuroimage.2017.09.019.

Girard, O.M., Prevost, V.H., Varma, G., Cozzone, P.J., Alsop, D.C., Duhamel, G., 2015. Magnetization transfer from inhomogeneously broadened lines (ihMT): experimental optimization of saturation parameters for human brain imaging at 1.5 Tesla. Magn. Reson. Med. 73, 2111–2121. doi:10.1002/mrm.25330.

Glasser, M.F., Van Essen, D.C., 2011. Mapping human cortical areas in vivo based on myelin content as revealed by T1- and T2-weighted MRI. J. Neurosci. 31, 11597–11616. doi:10.1523/JNEUROSCI.2180-11.2011.

Helms, G., Dathe, H., Kallenberg, K., Dechent, P., 2008. High-resolution maps of magnetization transfer with inherent correction for RF inhomogeneity and T1 relaxation obtained from 3D FLASH MRI. Magn. Reson. Med. 60, 1396–1407. doi:10.1002/mrm.21732.

Helms, G., Piringer, A., 2005. Simultaneous measurement of saturation and relaxation in human brain by repetitive magnetization transfer pulses. NMR Biomed. 18, 44–50. doi:10.1002/nbm.920.

Hilgetag, C.C., Barbas, H., 2006. Role of mechanical factors in the morphology of the primate cerebral cortex. PLoS Comput. Biol. 2, e22. doi:10.1371/journal.pcbi.0020022.

Horiuchi-Hirose, M., Sawada, K., 2016. Differential cortical laminar structure revealed by NeuN immunostaining and myeloarchitecture between sulcal and gyral regions independent of sexual dimorphisms in the ferret cerebrum. Anat. Rec. 299, 1003–1011. doi:10.1002/ar.23369.

Jang, H., Wei, Z., Wu, M., Ma, Y.-.J., Chang, E.Y., Corey-Bloom, J., Du, J., 2020. Improved volumetric myelin imaging in human brain using 3D dual echo inversion recovery-prepared UTE with complex echo subtraction. Magn. Reson. Med. 83, 1168–1177. doi:10.1002/mrm.28082.

Lee, Jongho, Hyun, J.-.W., Lee, Jieun, Choi, E.-.J., Shin, H.-.G., Min, K., Nam, Y., Kim, H.J., Oh, S.-.H., 2020. n.d. So you want to image Myelin using MRI: an overview and practical guide for myelin water imaging. J. Magn. Reson. Imaging doi:10.1002/jmri.27059.

Mangeat, G., Govindarajan, S.T., Mainero, C., Cohen-Adad, J., 2015. Multivariate combination of magnetization transfer, T2* and B0 orientation to study the myelo-architecture of the in vivo human cortex. Neuroimage 119, 89–102. doi:10.1016/j.neuroimage.2015.06.033.

Manning, A.P., Chang, K.L., MacKay, A.L., Michal, C.A., 2017. The physical mechanism of "inhomogeneous" magnetization transfer MRI. J. Magn. Reson. 274, 125–136. doi:10.1016/j.jmr.2016.11.013.

Marques, J.P., Khabipova, D., Gruetter, R., 2017. Studying cyto and myeloarchitecture of the human cortex at ultra-high field with quantitative imaging: R1, R2* and magnetic susceptibility. Neuroimage 147, 152–163. doi:10.1016/j.neuroimage.2016.12.009.

Mchinda, S., Varma, G., Prevost, V.H., Troter, A.L., Rapacchi, S., Guye, M., Pelletier, J., Ranjeva, J.-.P., Alsop, D.C., Duhamel, G., Girard, O.M., 2018. Whole brain inhomogeneous magnetization transfer (ihMT) imaging: Sensitivity enhancement within a steady-state gradient echo sequence. Magn. Reson. Med. 79, 2607–2619. doi:10.1002/mrm.26907.

Moll, N.M., Rietsch, A.M., Thomas, S., Ransohoff, A.J., Lee, J.-.C., Fox, R., Chang, A., Ransohoff, R.M., Fisher, E., 2011. Multiple sclerosis normal-appearing white matter: pathology–imaging correlations. Ann. Neurol. 70, 764–773. doi:10.1002/ana.22521.

Nieuwenhuys, R., 2013. The myeloarchitectonic studies on the human cerebral cortex of the vogt–vogt school, and their significance for the interpretation of functional neuroimaging data. Brain Struct. Funct. 218, 303–352. doi:10.1007/s00429-012-0460-z.

Prasloski, T., Rauscher, A., MacKay, A.L., Hodgson, M., Vavasour, I.M., Laule, C., Mädler, B., 2012. Rapid whole cerebrum myelin water imaging using a 3D GRASE sequence. Neuroimage 63, 533–539. doi:10.1016/j.neuroimage.2012.06.064.

Prevost, V.H., Girard, O.M., Mchinda, S., Varma, G., Alsop, D.C., Duhamel, G., 2017. Optimization of inhomogeneous magnetization transfer (ihMT) MRI contrast for preclinical studies using dipolar relaxation time (T1D) filtering. NMR Biomed. 30, e3706. doi:10.1002/nbm.3706.

Rowley, C.D., Bazin, P.-.L., Tardif, C.L., Sehmbi, M., Hashim, E., Zaharieva, N., Minuzzi, L., Frey, B.N., Bock, N.A., 2015. Assessing intracortical myelin in the living human brain using myelinated cortical thickness. Front. Neurosci. 9. doi:10.3389/fnins.2015.00396.

Sacolick, L.I., Wiesinger, F., Hancu, I., Vogel, M.W., 2010. B1 mapping by Bloch-Siegert shift. Magn. Reson. Med. 63, 1315–1322. doi:10.1002/mrm.22357.

Salat, D.H., Lee, S.Y., van der Kouwe, A.J., Greve, D.N., Fischl, B., Rosas, H.D., 2009. Age-associated alterations in cortical gray and white matter signal intensity and gray to white matter contrast. Neuroimage 48, 21–28. doi:10.1016/j.neuroimage.2009.06.074.

Sereno, M.I., Lutti, A., Weiskopf, N., Dick, F., 2013. Mapping the human cortical surface by combining quantitative T1 with retinotopy†. Cereb. Cortex 23, 2261–2268. doi:10.1093/cercor/bhs213.

Shafee, R., Buckner, R.L., Fischl, B., 2015. Gray matter myelination of 1555 human brains using partial volume corrected MRI images. Neuroimage 105, 473–485. doi:10.1016/j.neuroimage.2014.10.054.

Sprooten, E., O'Halloran, R., Dinse, J., Lee, W.H., Moser, D.A., Doucet, G.E., Goodman, M., Krinsky, H., Paulino, A., Rasgon, A., Leibu, E., Balchandani, P., Inglese, M., Frangou, S., 2019. Depth-dependent intracortical myelin organization in the living human brain determined by in vivo ultra-high field magnetic resonance imaging. Neuroimage 185, 27–34. doi:10.1016/j.neuroimage.2018.10.023.

Swanson, S.D., Malyarenko, D.I., Fabiilli, M.L., Welsh, R.C., Nielsen, J.-F., Srinivasan, A., 2017. Molecular, dynamic, and structural origin of inhomogeneous magnetization transfer in lipid membranes. Magn. Reson. Med. 77, 1318–1328. doi:10.1002/mrm.26210.

Uddin, M.N., Figley, T.D., Marrie, R.A., Figley, C.R., 2018. Can T1w/T2w ratio be used as a myelin-specific measure in subcortical structures? Comparisons between FSE-based T1w/T2w ratios, GRASE-based T1w/T2w ratios and multi-echo GRASE-based myelin water fractions. NMR Biomed. 31, e3868. doi:10.1002/nbm.3868.

Varma, G., Duhamel, G., Bazelaire, C.de, Alsop, D.C., 2015. Magnetization transfer from inhomogeneously broadened lines: a potential marker for myelin. Magn. Reson. Med. 73, 614–622. doi:10.1002/mrm.25174.

Varma, G., Girard, O.M., Mchinda, S., Prevost, V.H., Grant, A.K., Duhamel, G., Alsop, D.C., 2018. Low duty-cycle pulsed irradiation reduces magnetization transfer and increases the inhomogeneous magnetization transfer effect. J. Magn. Reson. 296, 60–71. doi:10.1016/j.jmr.2018.08.004.

Varma, G., Munsch, F., Burns, B., Duhamel, G., Girard, O.M., Guidon, A., Lebel, R.M., Alsop, D.C., 2020. Three-dimensional inhomogeneous magnetization transfer with rapid gradient-echo (3D ihMTRAGE) imaging. Magn. Reson. Med. doi:10.1002/mrm.28324.

Yarnykh, V.L., Bowen, J.D., Samsonov, A., Repovic, P., Mayadev, A., Qian, P., Gangadharan, B., Keogh, B.P., Maravilla, K.R., Jung Henson, L.K., 2014. Fast whole-brain three-dimensional macromolecular proton fraction mapping in multiple sclerosis. Radiology 274, 210–220. doi:10.1148/radiol.14140528.